

Cosmological Constraints using the Void Size Function Data from BOSS DR16

Yingxiao Song^{1,2}, Yan Gong^{1,2,3*}, Xingchen Zhou¹, Haitao Miao¹, Kwan Chuen Chan^{4,5},
and Xuelei Chen^{1,2,6,7}

¹National Astronomical Observatories, Chinese Academy of Sciences, 20A Datun Road, Beijing 100012, China

²School of Astronomy and Space Sciences, University of Chinese Academy of Sciences (UCAS), Yuquan Road NO.19A Beijing 100049, China

³Science Center for China Space Station Telescope, National Astronomical Observatories, Chinese Academy of Sciences, 20A Datun Road, Beijing 100101, China

⁴School of Physics and Astronomy, Sun Yat-sen University, 2 Daxue Road, Tangjia, Zhuhai, 519082, China

⁵CSST Science Center for the Guangdong-Hongkong-Macau Greater Bay Area, SYSU, Zhuhai, 519082, China

⁶Department of Physics, College of Sciences, Northeastern University, Shenyang 110819, China

⁷Centre for High Energy Physics, Peking University, Beijing 100871, China

Accepted XXX. Received YYY; in original form ZZZ

ABSTRACT

We measure the void size function (VSF) from the Baryon Oscillation Spectroscopic Survey (BOSS DR16) and perform the cosmological constraints. The BOSS DR16 galaxy sample is selected in the redshift range from $z = 0.2$ to 0.8 , considering the selection criteria based on galaxy number density. We identify non-spherical voids from this galaxy catalog using the Voronoi tessellation and watershed algorithm without assuming any void shape. We select the void samples based on the void ellipticity, and derive the VSFs in two redshift bins, i.e. $z = 0.2 - 0.5$ and $0.5 - 0.8$. The VSF model we use is based on the excursion-set theory, including the void linear underdensity threshold δ_v and the redshift space distortion (RSD) parameter B . The Markov Chain Monte Carlo (MCMC) method is applied to perform the joint constraints on the cosmological and void parameters. We find that the VSF measurement from BOSS DR16 gives $w = -1.263^{+0.329}_{-0.396}$, $\Omega_m = 0.293^{+0.060}_{-0.053}$, and $\sigma_8 = 0.897^{+0.159}_{-0.192}$, which can be a good complementary probe to galaxy clustering measurements. Our method demonstrates the potential of using the VSF to study cosmological models, and it can provide a reference for the future VSF analysis in the upcoming galaxy spectroscopic surveys.

Key words: Cosmology – Large-scale structure of Universe – Cosmological parameters

1 INTRODUCTION

In recent decades, our understanding of the cosmic large-scale structure (LSS), which describes the distribution of matter on cosmic scales, has advanced significantly. This progress has been primarily driven by extensive and high-precision galaxy surveys. As these surveys expand, they provide larger galaxy samples and increased survey volumes, which make the features of the LSS more recognizable. Among these features, cosmic voids, i.e. regions of space identified by a low density of galaxies in the LSS, are becoming increasingly important for studying the LSS and the evolution of the Universe. Various methods related to cosmic void for cosmological study have been discussed, such as the void abundance (e.g. Pollina et al. 2017, 2019; Contarini et al. 2021, 2022, 2023; Pelliciaro et al. 2023; Song et al. 2024a,b; Verza et al. 2024b,a), cross-correlation between void and other probes, e.g. galaxy clustering and gravitational lensing (e.g. Cai et al. 2016a; Sánchez et al. 2017b; Cautun et al. 2018; Nadathur & Percival 2019a; Vielzeuf et al. 2021; Woodfinden

et al. 2022; Bonici et al. 2023; Vielzeuf et al. 2023; Camacho-Ciurana et al. 2023; Mauland et al. 2023; Radinović et al. 2023; Song et al. 2024c, 2025).

As a powerful cosmological probe, cosmic void is effective for studying massive neutrinos and modified gravity (e.g. Cai et al. 2015; Pisani et al. 2015b; Zivick et al. 2015; Pollina et al. 2016; Achitouv 2016; Sahlén et al. 2016; Falck et al. 2018; Sahlén & Silk 2018; Paillas et al. 2019; Perico et al. 2019; Verza et al. 2019; Kreisch et al. 2019; Schuster et al. 2019; Kreisch et al. 2022; Verza et al. 2023; Thiele et al. 2024). Besides, the shape of cosmic voids is suitable for testing cosmological geometrical and dynamical effects due to their large volume, such as the baryonic acoustic oscillation (BAO) (e.g. Chan & Hamaus 2021; Forero-Sánchez et al. 2022; Khoraminezhad et al. 2022; Zhao et al. 2022; Tamone et al. 2023), redshift space distortion (RSD) (e.g. Paz et al. 2013; Cai et al. 2016b; Hamaus et al. 2017; Chuang et al. 2017; Nadathur & Percival 2019b; Nadathur et al. 2020; Correa et al. 2022) and Alcock-Paczynski (AP) effect (e.g. Sutter et al. 2012, 2014; Hamaus et al. 2016; Mao et al. 2017a; Correa et al. 2021; Hamaus et al. 2022; Radinović et al. 2024). Some important attempts using the observational data have demonstrated

* Email: gongyan@bao.ac.cn

the potential of cosmic voids for the cosmological study, and provided remarkable references for subsequent studies (e.g. Hamaus et al. 2016; Mao et al. 2017a,b; Hamaus et al. 2020; Nadathur et al. 2020; Aubert et al. 2022; Contarini et al. 2023; Thiele et al. 2024).

In this work, we derive the void size function (VSF), which characterizes the number density distribution of voids according to their size at a given redshift, from the sixteenth data release (DR16) of the Baryon Oscillation Spectroscopic Survey (BOSS, Dawson et al. 2013; Alam et al. 2015), contained within the sixteenth data release of the Sloan Digital Sky Survey (SDSS, Gunn et al. 2006; Ahumada et al. 2020), which also includes data from the Extended Baryon Oscillation Spectroscopic Survey (eBOSS, Dawson et al. 2016). The galaxy catalog from BOSS DR16 we use covers large contiguous sky areas and has a wide redshift coverage, which is ideal for the cosmological study using cosmic voids. We then use the VSF to investigate constraints on cosmological parameters.

The Sheth and van de Weygaert model (SvdW, Sheth & van de Weygaert 2004) was first used to describe the VSF. It assumes voids to be spherical in shape and forms the foundation of theoretical VSF models. The SvdW model was later extended to the volume-conserving model (Vdn, Jennings et al. 2013), which has become one of the most widely used VSF models.

We identify voids in galaxy catalog from BOSS DR16 using Voronoi tessellation and the watershed algorithm. The properties of the voids, such as the volume-weighted center, effective radius, and ellipticity, are estimated. These voids are identified to have arbitrary shapes, without assuming a simple spherical form. To ensure the reliability of our results, we select the voids based on the ellipticity criterion in our VSF analysis. The VSF data are derived in two redshift bins ranging from $z = 0.2$ to 0.8 . We employ the Markov Chain Monte Carlo (MCMC) method to constrain the model parameters. The theoretical model is based on the excursion-set theory, and includes the cosmological and void parameters. This method has been proven to be feasible and effective in the previous VSF analysis, which is tested using the mock data from simulations (Song et al. 2024a).

The paper is organized as follows: In Section 2, we introduce the galaxy catalog of BOSS DR16 we use, and the method for generating void catalogs; In Section 3, we discuss the calculation of the theoretical model and the estimation of the VSF data; In Section 4, we present the constraint results of the relevant cosmological and void parameters; The summary and conclusion are given in Section 5.

2 DATA ANALYSIS

2.1 Galaxy catalog

We use the galaxy catalog from BOSS DR16 (Dawson et al. 2013), which covers both the Northern and Southern Galactic Caps and includes galaxies from both BOSS DR12 and eBOSS DR16 (e.g. LOWZ and CMASS, Alam et al. 2017, 2021). This catalog covers a sky area of more than 10,000 square degrees and contains approximately four million sources with redshifts up to $z \sim 3$. To determine the accuracy of the redshift measurement of the sources, we choose the SPECTRA ANALYSIS & RETRIEVABLE CATALOG LAB¹ (SPARCL) to obtain the samples with SPECTYPE == GALAXY and ZWARN == 0. Here SPECTYPE is the classification of source, and ZWARN indicates the potential issues in the spectroscopic redshift measurement

¹ <https://astrosparcl.datalab.noirlab.edu/>

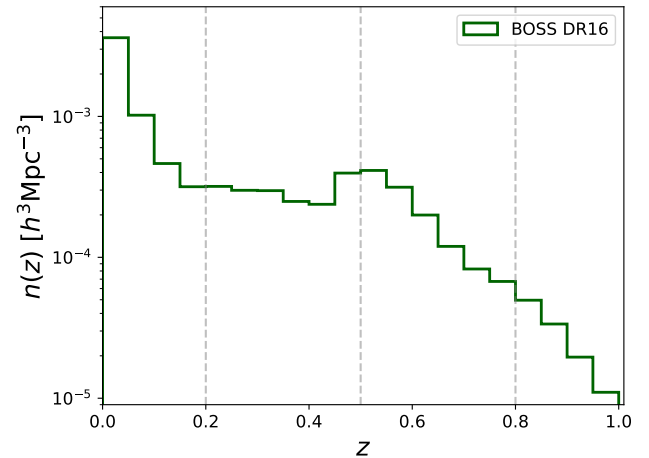


Figure 1. The galaxy number density distribution of our catalog from BOSS DR16 in $0 < z < 1$. The redshift bins are divided by the gray vertical dashed lines.

by a redshift fitting software Redrock². A total of 1,911,476 galaxies are retained in $0 < z < 2$. We assume a fiducial cosmology with $\Omega_m = 0.3111$ and $h = 0.6766$, based on the flat Λ CDM model and the Planck 2018 results (Planck Collaboration et al. 2020), to convert galaxy redshifts and angular positions into comoving coordinates and compute the relevant properties of galaxy and void, such as galaxy number density, mean galaxy separation, and void ellipticity. The galaxy number density distribution is shown in Figure 1.

Since the survey volume and number of galaxies are relatively small at $z < 0.2$, and the galaxy number density at $z > 0.8$ rapidly declines to the order of 10^{-5} , we selected two redshift ranges, i.e. $z = 0.2 - 0.5$ and $0.5 - 0.8$, based on the number density distribution in our galaxy catalog and previous studies (e.g. Reid et al. 2016; Hamaus et al. 2020; Zhao et al. 2022; Contarini et al. 2023). We calculate the number density of galaxies \bar{n}_g and the mean galaxy separation ($\text{MGS} = \bar{n}_g^{-1/3}$) by the number of galaxies N_g and the survey volume V_s at the two redshift bins. Note that the survey volume V_s is computed in the fiducial cosmology. We show the N_g , \bar{n}_g and MSG value in the two redshift bins in Table 1.

2.2 Void catalog

We use the Void IDentification and Examination toolkit³ (VIDE, Sutter et al. 2015) to obtain the void catalog from our galaxy catalog, with galaxy coordinates converted according to the fiducial cosmology. VIDE employs Voronoi tessellation and the watershed algorithm (Platen et al. 2007) to identify underdensity regions, based on the ZOnes Bordering On Voidness (ZOBOV) method (Neyrinck 2008). The voids identified by VIDE have the advantage of not assuming any specific shape, and it can provide several important void quantities, such as ellipticity, volume-weighted center, and effective radius. VIDE also can merge neighboring low-density regions based on the galaxy number density on the boundary, but in this work, we use the

² <https://github.com/desihub/redrock>

³ https://bitbucket.org/cosmicvoids/vid_public/src/master/

Table 1. The numbers and number densities of galaxy and void, i.e. N_g , N_v , \bar{n}_g and \bar{n}_v (in $h^3\text{Mpc}^{-3}$), in our catalog in the two redshift bins. The MGS, and minimum and maximum radius of voids (in $h^{-1}\text{Mpc}$) are also shown.

z_{\min}	z_{\max}	N_g	N_v	\bar{n}_g	\bar{n}_v	MGS	R_v^{\min}	R_v^{\max}
0.2	0.5	679834	3844	3.0×10^{-4}	1.7×10^{-6}	15	4	80
0.5	0.8	963604	5934	1.8×10^{-4}	1.1×10^{-6}	18	5	113

unmerged low-density zones to generate the void catalog for avoiding the void-in-void issue.

The void volume V and effective radius are calculated using the cell properties of the tracer, i.e. galaxy in our analysis. Voronoi tessellation assigns a cell to each galaxy, and the effective radius of the non-spherical void R_v is determined based on the volume of each cell V_{cell}^i in this void, that we have

$$R_v = \left(\frac{3V}{4\pi} \right)^{1/3} = \left(\frac{3}{4\pi} \sum_{i=1}^N V_{\text{cell}}^i \right)^{1/3}. \quad (1)$$

Here N is the number of cells in this void. We use the galaxy position \mathbf{x}_i in each cell to calculate the volume-weighted center of a void \mathbf{X}_v , which is given by

$$\mathbf{X}_v = \frac{\sum_{i=1}^N \mathbf{x}_i V_{\text{cell}}^i}{\sum_{i=1}^N V_{\text{cell}}^i}. \quad (2)$$

On the other hand, the irregularity of the void shape can be represented by the void ellipticity ϵ_v , which can be calculated from the maximum and minimum eigenvalues of the inertia tensor, i.e., I_{\max} and I_{\min} . Then we have

$$\epsilon_v = 1 - \left(\frac{I_{\min}}{I_{\max}} \right)^{1/4}. \quad (3)$$

The inertia tensor can be written as

$$I_{xx} = \sum_{i=1}^N (y_i^2 + z_i^2), \quad I_{xy} = -\sum_{i=1}^N x_i y_i. \quad (4)$$

Here I_{xy} and I_{xx} represent the off-diagonal and diagonal components, respectively, and x_i , y_i , and z_i are the galaxy coordinates in cell i measured relative to the void volume-weighted center \mathbf{X}_v . I_{yy} , I_{zz} , I_{xz} , and I_{yz} can be calculated using a similar formula to Equation (4).

We show the void ellipticity distribution in the two redshift bins in Figure 2. We can see that the two distributions of void ellipticity have a similar shape with a peak $\epsilon_v^{\text{peak}} \sim 0.15$. In Table 1, we show the number of voids N_v , void number densities and the minimum and maximum void radii in our catalog. We can find that, there is no order of magnitude difference in the number densities of galaxy and void between the two redshift bins, and the void and galaxy number densities decrease as the redshift increases, which is just as expected.

3 VOID SIZE FUNCTION

The void size function we adopt is based on the volume fraction conserving model, which is known as the Vdn model (Jennings et al. 2013). The VSF can be modeled by

$$\frac{dn_v}{d \ln R_v} = \left(\frac{3}{4\pi R_v^3} \right) \mathcal{F}(v, \delta_v, \delta_c) \frac{dv}{d \ln R_L}. \quad (5)$$

Here R_L is the void radius in Lagrangian space. In this framework, Lagrangian space refers to the initial, linearly evolved density field,

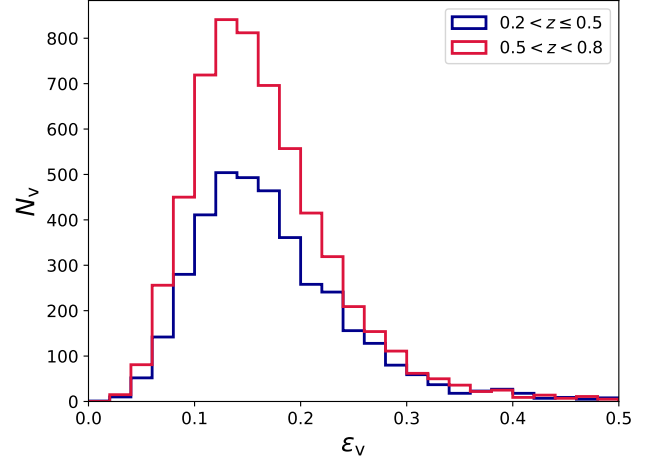


Figure 2. The void ellipticity distributions of the redshift bins $z = 0.2 - 0.5$ and $0.5 - 0.8$, respectively.

which is the linear density contrast as a function of position, scaled by the appropriate linear growth factor. This represents the density distribution at sufficiently high redshift, where linear theory accurately describes its statistical properties. On the other hand, Eulerian space describes the fully non-linear, evolved density field at the same redshift. In Equation (5), v is the significance of the void formation threshold in terms of the standard deviation of matter fluctuations (Desjacques et al. 2018), which is determined by the root-mean-square density fluctuations $\sigma_M(z)$ and the void formation threshold δ_v at different redshifts. It can be written as

$$v = \frac{|\delta_v|}{\sigma_M(z)}, \quad (6)$$

where $\sigma_M(z) = \sigma_0(R_L)D(z)$, and $D(z)$ is the linear growth factor. We use CAMB to obtain $\sigma_M(z)$ in our work (Lewis et al. 2000). $\mathcal{F}(v, \delta_v, \delta_c)$ denotes the probability that a random trajectory crosses the barrier δ_v for the first time at v without having crossed $\delta_c = 1.686$ for any $v' > v$. It can be calculated or approximated by (Sheth & van de Weygaert 2004)

$$\begin{aligned} \mathcal{F}(v, \delta_v, \delta_c) &= \frac{2\mathcal{D}^2}{v^3} \sum_{j=1}^{\infty} j\pi \sin(\mathcal{D}j\pi) \exp\left(-\frac{j^2\pi^2\mathcal{D}^2}{2v^2}\right) \\ &= \sqrt{\frac{2}{\pi}} \exp\left(-\frac{v^2}{2}\right) \exp\left(-\frac{|\delta_v|}{\delta_c} \frac{\mathcal{D}^2}{4v^2} - 2\frac{\mathcal{D}^4}{v^4}\right). \end{aligned} \quad (7)$$

Here $\mathcal{D} = |\delta_v|/(\delta_c + |\delta_v|)$. Note that, in early VSF studies, the theoretical value of δ_v was considered a fixed threshold, similar to the formation of halos (Jennings et al. 2013). However, more recent studies have shown that there is no strict theoretical threshold for void formation, and any negative value can be used, since voids are underdense regions defined by arbitrary density criteria (Pisani et al. 2015b; Nadathur & Hotchkiss 2015; Verza et al. 2019; Contarini

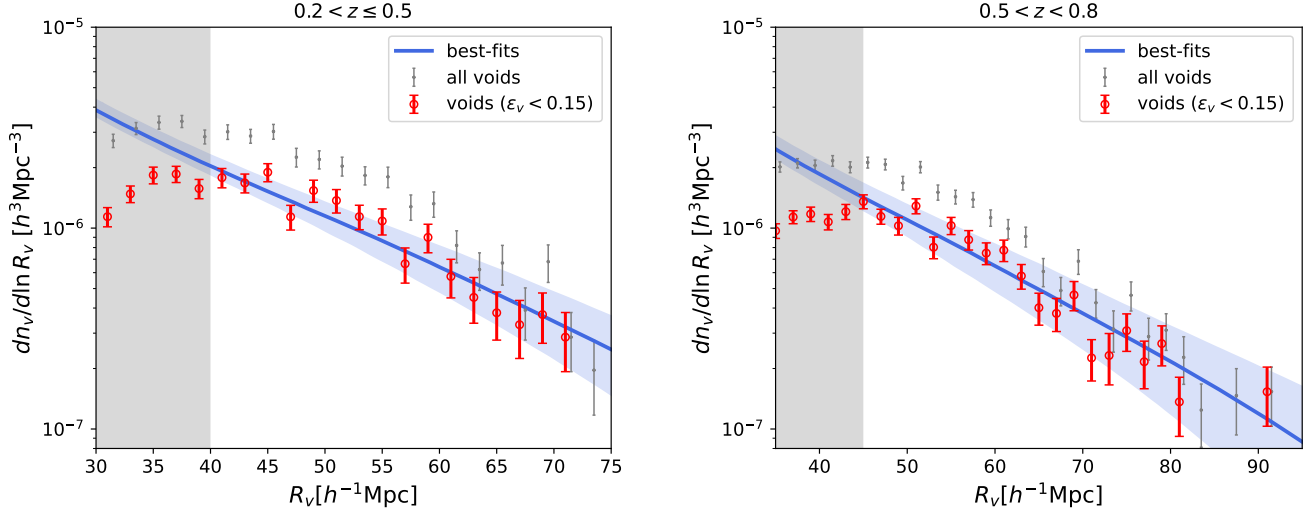


Figure 3. The void size functions from BOSS DR16 with $\epsilon_v < 0.15$ (red) and all voids (gray) in the two redshift bins. The blue curves are the best-fits of the theoretical VSF model obtained from the MCMC process, and the blue shaded regions indicate the uncertainty of the model calculated by using the 1σ errors of Ω_m and w . The gray areas represent the excluded scales based on $\sim 2.5 \times \text{MGS}$ in the fitting process.

et al. 2022; Verza et al. 2024b). Our voids are identified as low density regions with arbitrary shapes from our galaxy map using VIDE. Therefore, we take δ_v^i as a free parameter in the fitting process in the i th redshift bin to match the measured VSF data.

The mapping between the Lagrangian void size R_L and the Eulerian void size R_v can be derived based on the non-linear density contrast δ_v^{NL} , which reflects the transition from the linear to the non-linear regime. It is given by

$$R_L = R_v \left[\frac{\rho}{\rho_v} \right]^{-1/3} = \frac{R_v}{(1 + \delta_v^{\text{NL}})^{-1/3}}, \quad (8)$$

where ρ is the background matter density and ρ_v is the average density in a void. The relation between R_v and R_L can be estimated by

$$R_L \simeq \frac{R_v}{(1 - \delta_v/c_v)^{c_v/3}}, \quad (9)$$

where $c_v = 1.594$ and it represents the empirical best fit for the Lagrangian-to-Eulerian mapping in spherical symmetry (Bernardeau 1994; Jennings et al. 2013).

Since the volume and effective radius of voids identified in our catalog assuming the fiducial cosmology may deviate from that in the real observations, we need to consider the impact of redshift space distortions (RSD) and the Alcock-Paczynski (AP) effect (Alcock & Paczynski 1979) in our analysis. The RSD effect causes voids to appear larger due to the stretching along the line of sight (Pisani et al. 2015a; Zhao et al. 2016; Nadathur 2016; Correa et al. 2021). The AP effect introduces an anisotropy in the void shape, distorting the voids in both the parallel and perpendicular directions to the line of sight, since the true cosmology may deviate from the assumed fiducial cosmology. We use two factors, q_{RSD} and q_{AP} , to account for the corrections to the void radius from the RSD and AP effects, respectively, which are given by

$$R_v^{\text{obs}} = q_{\text{RSD}} q_{\text{AP}} R_v. \quad (10)$$

The AP effect is usually considered by applying scaling factors in both the radial and transverse directions (Correa et al. 2021), and we

have

$$\alpha_{\parallel} = \frac{H^{\text{fid}}(z)}{H(z)}, \quad \text{and} \quad \alpha_{\perp} = \frac{D_A(z)}{D_A^{\text{fid}}(z)}. \quad (11)$$

Here $H(z)$ and $D_A(z)$ represent the Hubble parameter and angular diameter distance, respectively, and the superscript “fid” denotes the values from the fiducial cosmology. We apply these two factors to correct the void radius affected by the AP effect, where $q_{\text{AP}} = \alpha_{\parallel}^{1/3} \alpha_{\perp}^{2/3}$ (Sánchez et al. 2017a; Hamaus et al. 2020; Correa et al. 2021; Contarini et al. 2023).

In our void sample used for analyzing the VSFs, the factor of RSD can be derived by (Correa et al. 2021)

$$q_{\text{RSD}} = 1 - \frac{1}{3} \delta R_v \beta \Delta(R_v), \quad (12)$$

where β is the ratio of the growth rate f to the galaxy bias b_g and δR_v is an additional factor that quantifies the variation in void radius, which is expected to range between 0 and 1 (Correa et al. 2021). We set $B^i = \beta^i \delta R_v^i$ as a free parameter in the i th redshift bin in the constraints. The value of $\Delta(R_v)$ can be computed using the formula $\Delta(R_v) = \delta_v^{\text{NL}} = (1 - \delta_v/c_v)^{-c_v} - 1$ (Bernardeau 1994).

Since the theoretical model of the VSF is based on the spherical evolution, and the voids identified by VIDE using the watershed algorithm have no assumed shape, we select spherical-like voids with the void ellipticity $\epsilon_v < 0.15$ in the fitting process. This selection criterion of the void ellipticity value is around the peak of the void ellipticity distributions in the two redshift bins as shown in Figure 2. We find the number of voids is reduced to around 45% for two redshift bins by applying this cut-off.

We should note that, in this analysis, since the void linear threshold δ_v is treated as a free parameter, it allows more flexibility in modeling the VSF. Moreover, the relation between the theoretical model based on the excursion-set model of Jennings et al. (2013) and the abundance derived from the observed watershed void catalog is empirical. A physically motivated theoretical model needs to be constructed to describe the watershed voids more precisely, which will be explored in the future.

We show the void size functions for all voids and voids with

$\epsilon_v < 0.15$ of the two redshift bins in Figure 3. We notice that, since the ellipticity of small-size voids is relatively high (Song et al. 2024a), the difference between the theoretical model and data at small scales generally cannot be ignored. Previous studies usually exclude the small-size voids based on the value of MGS (e.g. Ronconi et al. 2019; Contarini et al. 2019, 2021, 2022, 2023, 2024). We follow this method and exclude voids with $R_v < 40h^{-1}\text{Mpc}$ in $0.2 < z \leq 0.5$ and $R_v < 45h^{-1}\text{Mpc}$ in $0.5 < z < 0.8$, which are approximately 2.5 times of the MGS in the two redshift bins. Furthermore, if the number of voids is less than 5 in a void radius bin, we exclude them in the fitting process to ensure the statistical significance.

To test the robustness of our selection criteria, we conducted tests on the ellipticity cut for each redshift bin. We find that for ellipticity thresholds of $\epsilon_v = 0.14$ or 0.16 , the constraint result would not change significantly and is consistent with the case using $\epsilon_v = 0.15$. However, if choosing a threshold smaller than 0.14 or larger than 0.16 , it leads to deviations of more than 1σ in some parameters (e.g. Ω_m). This suggests that moderate change of the ellipticity cut is acceptable in our method, and the result is not very sensitive to this cut. And we also find that our selection includes all approximately spherical large-size voids with ellipticity below the mean value of the sample. Therefore, we consider that our current ellipticity selection criterion, which is based on the peak value from the void ellipticity distribution, provides a reasonable choice.

Note that the trimming on void ellipticity is empirically motivated. There is currently no theoretical framework that can provide an optimal ellipticity threshold to select voids corresponding to the assumptions of the Jennings et al. (2013) model. Based on the analysis in this work and our previous work (Song et al. 2024a), we notice that the void ellipticity distribution is size-dependent, that larger voids tend to be more spherical while smaller voids are more flattened. This trend suggests that the future theoretical models could include size-dependent terms for helping introducing priors on the ellipticity choice to improve the robustness of cosmological constraints.

In addition, we also test different minimum void radius selections in each redshift bin to evaluate their impact on the constraints. We firstly examine two choices, i.e. one with a radius $5 h^{-1}\text{Mpc}$ smaller ($\sim 2.3 \times \text{MGS}$) and another with a $10 h^{-1}\text{Mpc}$ smaller radius ($\sim 2 \times \text{MGS}$) than our current choice of $\sim 2.5 \times \text{MGS}$. We find that both of these choices have significant impact on the constraints, that the results deviate by more than 1σ for some parameters, e.g. Ω_m , w and δ_v , compared to the results from the case with $\sim 2.5 \times \text{MGS}$. On the other hand, if we choose larger void radius cuts, the best-fit results of the model parameters would not change significantly, but the errors will become larger, since less data points are used in the fitting process in this case. Based on these tests, we consider that our current selection of the minimum void radius ($\sim 2.5 \times \text{MGS}$) is reasonable and can provide reliable constraint results. Besides, this minimum void radius is also consistent with the selection used in previous studies (e.g. Ronconi et al. 2019; Contarini et al. 2019, 2021, 2023, 2024).

In order to estimate the uncertainty in the VSF measurements, we calculate the covariance matrix using the jackknife method. The advantage of the jackknife method is that it estimates the statistical uncertainty directly from the observational catalog, using the same assumed cosmology for both the measured void size function and its covariance. Although the measurement still depends on the fiducial cosmology used to convert redshifts into distances, the method ensures consistency between the measured VSF and its error estimate. In addition, the covariance matrix estimated using the jackknife method converges to the true covariance matrix in the limit of large volume (Favole et al. 2021).

We apply the method of equally dividing the sky area to generate

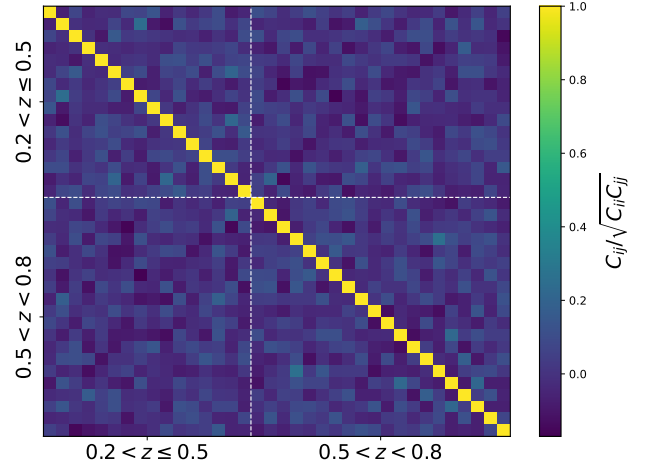


Figure 4. The normalized covariance matrix of the void size function by its diagonal components. The two redshift bins are separated by the vertical and horizontal white dashed lines.

the jackknife subsamples for a more accurate error estimate (Zhou et al. 2021), and use 200 subsamples to compute the covariance matrix. In Figure 3, we compare the measured void size functions from BOSS DR16 with the best-fit model derived from the MCMC sampling. The uncertainty of the best-fit curve derived from the 1σ errors of Ω_m and w is also shown in shaded blue region in each redshift bin. The error bars for each data point in Figure 3 are calculated from the square root of the diagonal elements of the covariance matrix. Figure 4 shows the covariance matrix C_{ij} normalized by its diagonal components $\sqrt{C_{ii}C_{jj}}$.

4 CONSTRAINT AND RESULTS

We adopt the standard likelihood function $\mathcal{L} \propto \exp(-\chi^2/2)$ for the model fitting, and the χ^2 is given by

$$\chi^2 = \left[n_v^{\text{obs}}(R_v) - n_v^{\text{th}}(R_v) \right]^T \mathbf{C}^{-1} \left[n_v^{\text{obs}}(R_v) - n_v^{\text{th}}(R_v) \right], \quad (13)$$

where $n_v^{\text{obs}}(R_v)$ is the measured VSF data, $n_v^{\text{th}}(R_v) = dn_v/d \ln R_v$ is the modeled VSF as shown in Equation (5), and \mathbf{C} is the covariance matrix of the measured VSF. In our fitting process, we use the $n_v(R_v)$ from the two redshift bins to obtain the joint constraint result. We employ the MCMC method by applying emcee (Foreman-Mackey et al. 2013; Goodman & Weare 2010) to constrain the free parameters in our model. We obtain over 1 million chain points, and remove the first 10% of the steps as the burn-in process. Then we randomly select 10,000 points for thinning the chains to illustrate the probability distribution functions (PDFs) of the free parameters.

In our analysis, we adopt the w -cold dark matter ($w\text{CDM}$) model and focus on the total matter density parameter Ω_m , the dark energy equation of state w and the amplitude of matter density fluctuations on a scale of $8 h^{-1}\text{Mpc}$, σ_8 . To improve the constraints on the three parameters we are interested in, we apply a 10σ Gaussian prior to the remaining cosmological parameters, such as the reduced Hubble constant h , baryon density parameter Ω_b , and spectral index n_s , the amplitude of the initial power spectrum A_s , based on the results from Planck2018 (Planck Collaboration et al. 2020). These priors are reasonable and consistent with other observations and analyses (e.g. Aver et al. 2015; Cooke et al. 2018; Schöneberg et al. 2019;

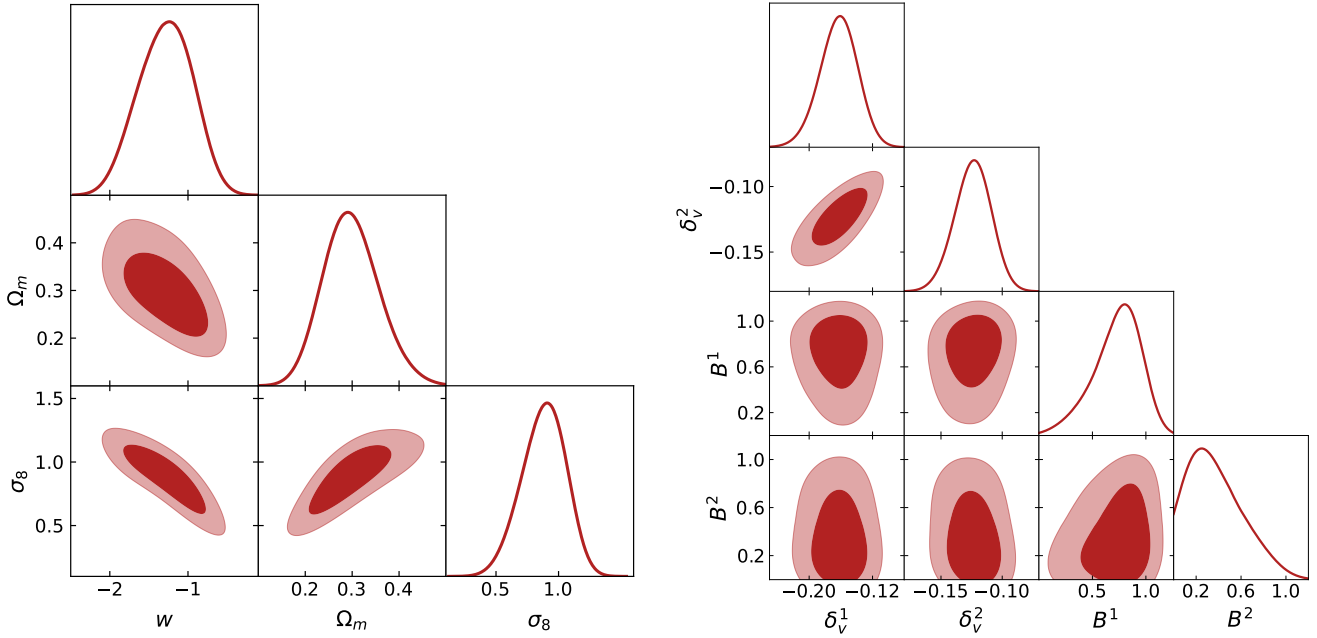


Figure 5. The 1D PDFs and contour maps at 68% and 95% CL for w , Ω_m , and σ_8 (left panel), and δ_v^i and B^i in the two redshift bins (right panel), using the VSF data from BOSS DR16 data.

Alam et al. 2017, 2021; Philcox & Ivanov 2022; Contarini et al. 2023). Note that we convert A_s and derive the constraint result of σ_8 from the chain points.

In addition to these cosmological parameters, we also consider four other parameters, including the void linear underdensity threshold parameter δ_v and the RSD parameter B in the two redshift bins. We constrain all the parameters simultaneously in the fitting process. The priors and constraint results for all the free parameters are shown in Table 2.

In the left panel of Figure 5, we show the 1D PDFs and contour maps at 68% and 95% confidence level (CL) of Ω_m , w and σ_8 . We can find that the cosmological parameters are well constrained with accuracies $w \sim 29\%$, $\Omega_m \sim 19\%$, $\sigma_8 \sim 20\%$, and the 1σ CLs are consistent with the previous results from BOSS DR12 (e.g. Contarini et al. 2023). We notice that the constraints on w and Ω_m are comparable to those obtained using the VSFs from BOSS DR12, although we use the non-spherical void samples to fit the VSF model and have more free parameters. The constraint on σ_8 is relatively weak, due to more free parameters are considered and more flexible priors are assumed in our work. These results indicate that our approach of selecting voids based on void ellipticity and MGS values is effective for obtaining reliable VSF data. The constraint results for all free parameters are presented in the Appendix A.

We also note that the degeneracy directions of the $\Omega_m - \sigma_8$, $\Omega_m - w$ and $w - \sigma_8$ contours are consistent with the previous work using mock catalogs (e.g. Contarini et al. 2022). And the degeneracy direction of $\Omega_m - \sigma_8$ contour is almost orthogonal to that obtained from other probes, such as galaxy clustering and the halo mass function (e.g., Contarini et al. 2022; Pellicciari et al. 2023). This suggests that the VSF measurement can be complementary to the probes for overdense regions, e.g. galaxy clustering, and could effectively break the degeneracies of the relevant parameters in the joint analysis.

To check the effect of the 10σ Gaussian priors of h , Ω_b , and n_s on the constraint results, we also consider the 1σ Planck2018 Gaussian priors for the three parameters. In this case, we find that

$w = -1.081^{+0.271}_{-0.397}$, $\Omega_m = 0.323^{+0.064}_{-0.060}$ and $\sigma_8 = 0.873^{+0.174}_{-0.196}$. We can see that the constraint results of the two cases are consistent in 1σ and the constraint accuracies are similar, although the best-fit values of w and Ω_m from the 1σ prior case are closer to the Planck2018 results. This means that our constraint result is not sensitive to the choice of the Gaussian priors of h , Ω_b , and n_s . The contour maps for the 1σ Gaussian prior case are shown in the Appendix A.

Our results show that the void size function is sensitive to the cosmological parameters Ω_m , σ_8 , and w , which directly affect the amplitude and growth of matter density fluctuations. In contrast, parameters such as n_s , h , and Ω_b are poorly constrained by the VSF, and varying their priors has insignificant impact on the posteriors of Ω_m , σ_8 , and w . The weak impact arises from the fact that these parameters have limited influence on the large-scale structure at the scales probed by voids. The Ω_b affects baryon acoustic oscillations in the matter power spectrum but has little impact on its overall shape and amplitude at void-relevant scales. The n_s mainly affects the shape of the power spectrum at very large scales (low k) beyond typical void sizes. The h has degeneracies with other parameters, such as the free parameter B in the RSD effect, which makes it poorly constrained and insensitive to the constraint results of Ω_m , σ_8 , and w .

In the right panel of Figure 5, we show the results for the linear underdensity thresholds for void formation δ_v^i and the RSD parameter B^i in the two redshift bins. The best-fit values and 1σ errors for δ_v^i and B^i in each redshift bin are listed in Table 2. We find that δ_v^i is well constrained, with the accuracy smaller than 15%. The constraint on B^i are weak, and the best-fit value of B decreases as redshift increases, which is basically due to that the galaxy bias increases at larger redshifts.

We also find that the best-fit values of δ_v are ranging from ~ -0.2 to -0.1 in the two redshift bins, which increase with redshift. This is consistent with the previous study using the mock VSF data from simulations (Song et al. 2024a). It is mainly because that our voids are identified by the watershed algorithm without assuming the spherical shape, and our void tracers are galaxies, i.e. biased objects, instead

Table 2. The priors and constraint results of the cosmological parameters, the void linear underdensity threshold parameter δ_v^i and RSD parameter B^i in the two redshift bins. Note that $\mathcal{U}(a, b)$ denotes a uniform prior with the range (a, b) , and $\mathcal{N}(\mu, \sigma)$ indicates a Gaussian prior, where μ and σ are the mean value and standard deviation, respectively.

Parameter	Prior	Constraint Results
Cosmology		
w	$\mathcal{U}(-2.0, 0)$	$-1.263^{+0.329}_{-0.396}$
Ω_m	$\mathcal{U}(0.1, 0.5)$	$0.293^{+0.060}_{-0.053}$
σ_8	-	$0.897^{+0.159}_{-0.192}$
$A_s (\times 10^{-9})$	$\mathcal{N}(2.105, 0.3)$	$2.181^{+0.293}_{-0.297}$
h	$\mathcal{N}(0.6766, 0.042)$	$0.711^{+0.033}_{-0.032}$
Ω_b	$\mathcal{N}(0.049, 0.003)$	0.049 ± 0.003
n_s	$\mathcal{N}(0.9665, 0.038)$	$0.971^{+0.037}_{-0.038}$
Void		
δ_v^1	$\mathcal{U}(-2.0, 0)$	$-0.162^{+0.022}_{-0.024}$
δ_v^2	$\mathcal{U}(-2.0, 0)$	$-0.123^{+0.014}_{-0.015}$
RSD		
B^1	$\mathcal{U}(0, 1.0)$	$0.777^{+0.160}_{-0.267}$
B^2	$\mathcal{U}(0, 1.0)$	$0.289^{+0.335}_{-0.209}$

of the particles. Additionally, the increasing trend of δ_v is due to that the void size becomes larger (as shown in Figure 3) and the evolution of voids is more linear at higher redshifts, which means the Eulerian void size R_v becomes closer and closer to the Lagrangian void size R_L as redshift increasing. As shown in Equation (9), this will make δ_v closer to 0 from low to high redshifts. Besides, we notice that the best-fit values of δ_v from BOSS DR16 are higher than that from the mock data given in Song et al. (2024a), which is caused by the lower galaxy number density and larger void size in the BOSS DR16 data.

We also investigate the constraint on δ_v^i and B^i from the 1σ Planck2018 Gaussian prior case, and find that $\delta_v^1 = -0.150^{+0.017}_{-0.018}$ and $\delta_v^2 = -0.116^{+0.011}_{-0.011}$. We can find that the constraint results of the four parameters are in good agreement for both cases. The best-fit value of δ_v^i from the 1σ prior case slightly increase compared to the 10σ prior case, with a relative accuracy improvement of about 20%, while the results for B^i are similar for the two cases. The constraint results of the δ_v^i and B^i from the 1σ prior case are shown in the Appendix A.

5 SUMMARY AND CONCLUSION

In this work, we investigate the void size function measured from BOSS DR16, and explore the constraints on the cosmological and void parameters. We identify voids in the BOSS DR16 galaxy catalog at $0.2 < z < 0.8$ by employing Voronoi tessellation and the watershed algorithm without assuming the spherical shape. The voids with the ellipticity $\epsilon_v < 0.15$ are selected, and the small-size voids which are smaller than $2.5 \times \text{MGS}$ value in a redshift bin are excluded. Then the

void catalog and the VSFs in the two redshift bins are derived for the cosmological constraint.

We utilize the MCMC method to jointly constrain the cosmological and void parameters, and assume 10σ Gaussian priors from Planck18 results for A_s , h , Ω_b , and n_s . We obtain $w = -1.263^{+0.329}_{-0.396}$, $\Omega_m = 0.293^{+0.060}_{-0.053}$, and $\sigma_8 = 0.897^{+0.159}_{-0.192}$, which are in good agreement with the results from BOSS DR12 data. Besides, we find that the degeneracy direction of $\Omega_m - \sigma_8$ from the VSF is almost orthogonal to that from the galaxy clustering and halo mass function measurements. This indicates that the VSF can be an effective complementary probe to the probes for the overdense regions. In addition, the best-fit value of the void linear threshold parameter δ_v increases and is close to 0 at higher redshifts, which is reasonable and consistent with the previous study using the similar method applied to the mock data from simulations.

The VSF probe can be more important in the ongoing and upcoming galaxy surveys that can perform spectroscopic measurements, such as the Dark Energy Spectroscopic Instrument (DESI, DESI Collaboration et al. 2016), 4-metre Multi-Object Spectroscopic Telescope (4MOST, de Jong et al. 2019; Walcher et al. 2019), Multiplexed Survey Telescope (MUST, Zhao et al. 2024), Nancy Grace Roman Space Telescope (RST, Akeson et al. 2019), Euclid (Euclid Collaboration et al. 2022), and China Space Station Telescope (CSST, Zhan 2011, 2021; Gong et al. 2019; Miao et al. 2023). These surveys are expected to greatly increase the number of observed galaxies and voids by one or two orders of magnitude compared to BOSS, and the constraint accuracy of the cosmological parameters also can be significantly improved. Our VSF method also can provide a reference for the void analysis in the next-generation galaxy surveys.

ACKNOWLEDGEMENTS

YS and YG acknowledge the support from National Key R&D Program of China grant Nos. 2022YFF0503404, 2020SKA0110402, and the CAS Project for Young Scientists in Basic Research (No. YSBR-092). KCC acknowledges the support the National Science Foundation of China under the grant number 12273121. XLC acknowledges the support of the National Natural Science Foundation of China through Grant Nos. 12361141814, and the Chinese Academy of Science grants ZDKYYQ20200008. This work was also supported by science research grants from the China Manned Space Project with grant nos. CMS-CSST-2025-A02, CMS-CSST-2021-B01 and CMS-CSST-2021-A01.

DATA AVAILABILITY

The data that support the findings of this study are available from the corresponding author upon reasonable request.

REFERENCES

- Achitouv I., 2016, *Phys. Rev. D*, 94, 103524
 Ahumada R., et al., 2020, *ApJS*, 249, 3
 Akeson R., et al., 2019, *arXiv e-prints*, p. arXiv:1902.05569
 Alam S., et al., 2015, *ApJS*, 219, 12
 Alam S., et al., 2017, *MNRAS*, 470, 2617
 Alam S., et al., 2021, *Phys. Rev. D*, 103, 083533
 Alcock C., Paczynski B., 1979, *Nature*, 281, 358
 Aubert M., et al., 2022, *MNRAS*, 513, 186

- Aver E., Olive K. A., Skillman E. D., 2015, *J. Cosmology Astropart. Phys.*, 2015, 011
- Bernardeau F., 1994, *ApJ*, 427, 51
- Bonici M., et al., 2023, *A&A*, 670, A47
- Cai Y.-C., Padilla N., Li B., 2015, *MNRAS*, 451, 1036
- Cai Y.-C., Taylor A., Peacock J. A., Padilla N., 2016a, *MNRAS*, 462, 2465
- Cai Y.-C., Taylor A., Peacock J. A., Padilla N., 2016b, *MNRAS*, 462, 2465
- Camacho-Ciurana G., Lee P., Arsenov N., Kovács A., Szapudi I., Csabai I., 2023, *arXiv e-prints*, p. arXiv:2312.08483
- Cautun M., Paillas E., Cai Y.-C., Bose S., Armijo J., Li B., Padilla N., 2018, *MNRAS*, 476, 3195
- Chan K. C., Hamaus N., 2021, *Phys. Rev. D*, 103, 043502
- Chuang C.-H., Kitaura F.-S., Liang Y., Font-Ribera A., Zhao C., McDonald P., Tao C., 2017, *Phys. Rev. D*, 95, 063528
- Contarini S., Ronconi T., Marulli F., Moscardini L., Veropalumbo A., Baldi M., 2019, *MNRAS*, 488, 3526
- Contarini S., Marulli F., Moscardini L., Veropalumbo A., Giocoli C., Baldi M., 2021, *MNRAS*, 504, 5021
- Contarini S., et al., 2022, *A&A*, 667, A162
- Contarini S., Pisani A., Hamaus N., Marulli F., Moscardini L., Baldi M., 2023, *ApJ*, 953, 46
- Contarini S., Pisani A., Hamaus N., Marulli F., Moscardini L., Baldi M., 2024, *A&A*, 682, A20
- Cooke R. J., Pettini M., Steidel C. C., 2018, *ApJ*, 855, 102
- Correa C. M., Paz D. J., Sánchez A. G., Ruiz A. N., Padilla N. D., Angulo R. E., 2021, *MNRAS*, 500, 911
- Correa C. M., Paz D. J., Padilla N. D., Sánchez A. G., Ruiz A. N., Angulo R. E., 2022, *MNRAS*, 509, 1871
- DESI Collaboration et al., 2016, *arXiv e-prints*, p. arXiv:1611.00036
- Dawson K. S., et al., 2013, *AJ*, 145, 10
- Dawson K. S., et al., 2016, *AJ*, 151, 44
- Desjacques V., Jeong D., Schmidt F., 2018, *Phys. Rep.*, 733, 1
- Euclid Collaboration et al., 2022, *A&A*, 662, A112
- Falck B., Koyama K., Zhao G.-B., Cautun M., 2018, *MNRAS*, 475, 3262
- Favole G., Granett B. R., Silva Laffaurie J., Sapone D., 2021, *MNRAS*, 505, 5833
- Foreman-Mackey D., Hogg D. W., Lang D., Goodman J., 2013, *PASP*, 125, 306
- Forero-Sánchez D., Zhao C., Tao C., Chuang C.-H., Kitaura F.-S., Variu A., Tamone A., Kneib J.-P., 2022, *MNRAS*, 513, 5407
- Gong Y., et al., 2019, *ApJ*, 883, 203
- Goodman J., Weare J., 2010, *Communications in Applied Mathematics and Computational Science*, 5, 65
- Gunn J. E., et al., 2006, *AJ*, 131, 2332
- Hamaus N., Pisani A., Sutter P. M., Lavaux G., Escoffier S., Wandelt B. D., Weller J., 2016, *Phys. Rev. Lett.*, 117, 091302
- Hamaus N., Cosinou M.-C., Pisani A., Aubert M., Escoffier S., Weller J., 2017, *J. Cosmology Astropart. Phys.*, 2017, 014
- Hamaus N., Pisani A., Choi J.-A., Lavaux G., Wandelt B. D., Weller J., 2020, *J. Cosmology Astropart. Phys.*, 2020, 023
- Hamaus N., et al., 2022, *A&A*, 658, A20
- Jennings E., Li Y., Hu W., 2013, *MNRAS*, 434, 2167
- Khoramizhad H., Vielzeuf P., Lazeyras T., Baccigalupi C., Viel M., 2022, *MNRAS*, 511, 4333
- Kreisch C. D., Pisani A., Carbone C., Liu J., Hawken A. J., Massara E., Spergel D. N., Wandelt B. D., 2019, *MNRAS*, 488, 4413
- Kreisch C. D., Pisani A., Villaescusa-Navarro F., Spergel D. N., Wandelt B. D., Hamaus N., Bayer A. E., 2022, *ApJ*, 935, 100
- Lewis A., Challinor A., Lasenby A., 2000, *ApJ*, 538, 473
- Mao Q., Berlind A. A., Scherrer R. J., Neyrinck M. C., Scoccamarro R., Tinker J. L., McBride C. K., Schneider D. P., 2017a, *ApJ*, 835, 160
- Mao Q., et al., 2017b, *ApJ*, 835, 161
- Mauland R., Elgarøy Ø., Mota D. F., Winther H. A., 2023, *A&A*, 674, A185
- Miao H., Gong Y., Chen X., Huang Z., Li X.-D., Zhan H., 2023, *MNRAS*, 519, 1132
- Nadathur S., 2016, *MNRAS*, 461, 358
- Nadathur S., Hotchkiss S., 2015, *MNRAS*, 454, 2228
- Nadathur S., Percival W. J., 2019a, *MNRAS*, 483, 3472
- Nadathur S., Percival W. J., 2019b, *MNRAS*, 483, 3472
- Nadathur S., et al., 2020, *MNRAS*, 499, 4140
- Neyrinck M. C., 2008, *MNRAS*, 386, 2101
- Paillas E., Cautun M., Li B., Cai Y.-C., Padilla N., Armijo J., Bose S., 2019, *MNRAS*, 484, 1149
- Paz D., Lares M., Ceccarelli L., Padilla N., Lambas D. G., 2013, *MNRAS*, 436, 3480
- Pellicciari D., Contarini S., Marulli F., Moscardini L., Giocoli C., Lesci G. F., Dolag K., 2023, *MNRAS*, 522, 152
- Perico E. L. D., Voivodic R., Lima M., Mota D. F., 2019, *A&A*, 632, A52
- Philcox O. H. E., Ivanov M. M., 2022, *Phys. Rev. D*, 105, 043517
- Pisani A., Sutter P. M., Wandelt B. D., 2015a, *arXiv e-prints*, p. arXiv:1506.07982
- Pisani A., Sutter P. M., Hamaus N., Alizadeh E., Biswas R., Wandelt B. D., Hirata C. M., 2015b, *Phys. Rev. D*, 92, 083531
- Planck Collaboration et al., 2020, *A&A*, 641, A6
- Platen E., van de Weygaert R., Jones B. J. T., 2007, *MNRAS*, 380, 551
- Pollina G., Baldi M., Marulli F., Moscardini L., 2016, *MNRAS*, 455, 3075
- Pollina G., Hamaus N., Dolag K., Weller J., Baldi M., Moscardini L., 2017, *MNRAS*, 469, 787
- Pollina G., et al., 2019, *MNRAS*, 487, 2836
- Radinović S., et al., 2023, *A&A*, 677, A78
- Radinović S., Winther H. A., Nadathur S., Percival W. J., Paillas E., Sohrab Fraser T., Massara E., Woodfinden A., 2024, *A&A*, 691, A39
- Reid B., et al., 2016, *MNRAS*, 455, 1553
- Ronconi T., Contarini S., Marulli F., Baldi M., Moscardini L., 2019, *MNRAS*, 488, 5075
- Sahlén M., Silk J., 2018, *Phys. Rev. D*, 97, 103504
- Sahlén M., Zubeldía Í., Silk J., 2016, *ApJ*, 820, L7
- Sánchez A. G., et al., 2017a, *MNRAS*, 464, 1640
- Sánchez C., et al., 2017b, *MNRAS*, 465, 746
- Schöneberg N., Lesgourgues J., Hooper D. C., 2019, *J. Cosmology Astropart. Phys.*, 2019, 029
- Schuster N., Hamaus N., Pisani A., Carbone C., Kreisch C. D., Pollina G., Weller J., 2019, *J. Cosmology Astropart. Phys.*, 2019, 055
- Sheth R. K., van de Weygaert R., 2004, *MNRAS*, 350, 517
- Song Y., et al., 2024a, *MNRAS*, 532, 1049
- Song Y., et al., 2024b, *MNRAS*, 534, 128
- Song Y., et al., 2024c, *ApJ*, 976, 244
- Song Y., Gong Y., Xiong Q., Chan K. C., Chen X., Guo Q., Liu Y., Pei W., 2025, *MNRAS*, 538, 114
- Sutter P. M., Lavaux G., Wandelt B. D., Weinberg D. H., 2012, *ApJ*, 761, 187
- Sutter P. M., Pisani A., Wandelt B. D., Weinberg D. H., 2014, *MNRAS*, 443, 2983
- Sutter P. M., et al., 2015, *Astronomy and Computing*, 9, 1
- Tamone A., Zhao C., Forero-Sánchez D., Variu A., Chuang C.-H., Kitaura F.-S., Kneib J.-P., Tao C., 2023, *MNRAS*, 526, 2889
- Thiele L., Massara E., Pisani A., Hahn C., Spergel D. N., Ho S., Wandelt B., 2024, *ApJ*, 969, 89
- Verza G., Pisani A., Carbone C., Hamaus N., Guzzo L., 2019, *J. Cosmology Astropart. Phys.*, 2019, 040
- Verza G., Carbone C., Pisani A., Renzi A., 2023, *J. Cosmology Astropart. Phys.*, 2023, 044
- Verza G., et al., 2024a, *arXiv e-prints*, p. arXiv:2410.19713
- Verza G., Carbone C., Pisani A., Porciani C., Matarrese S., 2024b, *J. Cosmology Astropart. Phys.*, 2024, 079
- Vielzeuf P., et al., 2021, *MNRAS*, 500, 464
- Vielzeuf P., Calabrese M., Carbone C., Fabbian G., Baccigalupi C., 2023, *J. Cosmology Astropart. Phys.*, 2023, 010
- Walcher C. J., et al., 2019, *The Messenger*, 175, 12
- Woodfinden A., Nadathur S., Percival W. J., Radinovic S., Massara E., Winther H. A., 2022, *MNRAS*, 516, 4307
- Zhan H., 2011, *Scientia Sinica Physica, Mechanica & Astronomica*, 41, 1441
- Zhan H., 2021, *Chinese Science Bulletin*, 66, 1290
- Zhao C., Tao C., Liang Y., Kitaura F.-S., Chuang C.-H., 2016, *MNRAS*, 459, 2670
- Zhao C., et al., 2022, *MNRAS*, 511, 5492
- Zhao C., et al., 2024, *arXiv e-prints*, p. arXiv:2411.07970

- Zhou R., et al., 2021, *MNRAS*, 501, 3309
 Zivick P., Sutter P. M., Wandelt B. D., Li B., Lam T. Y., 2015, *MNRAS*, 451, 4215
 de Jong R. S., et al., 2019, *The Messenger*, 175, 3

APPENDIX A: MCMC RESULTS AND THE EFFECT OF PRIORS

In Figure A1, we show the 1D PDFs and contour maps at 68% and 95% CL for all the free parameters in the model. The details of the priors, best-fit values and 1σ errors for the cosmological parameters, as well as the linear underdensity thresholds for void formation δ_v^i and RSD parameter B^i in the two redshift bins are shown in Table 2.

In order to check the impact of the assumed Gaussian priors of h , Ω_b , and n_s on the cosmological constraint, we also apply stronger priors, i.e., 1σ Gaussian priors from *Planck2018*, for h , Ω_b and n_s . This choice is almost equivalent to fix the values of h , Ω_b , and n_s , since the 1σ errors from *Planck2018* are extremely small compared to that from the VSF measurement. Our results for the cosmological parameters, which include w , Ω_m , σ_8 , and the four nuisance parameters δ_v and B from the two redshift bins are displayed in Figure A2.

This paper has been typeset from a \LaTeX file prepared by the author.

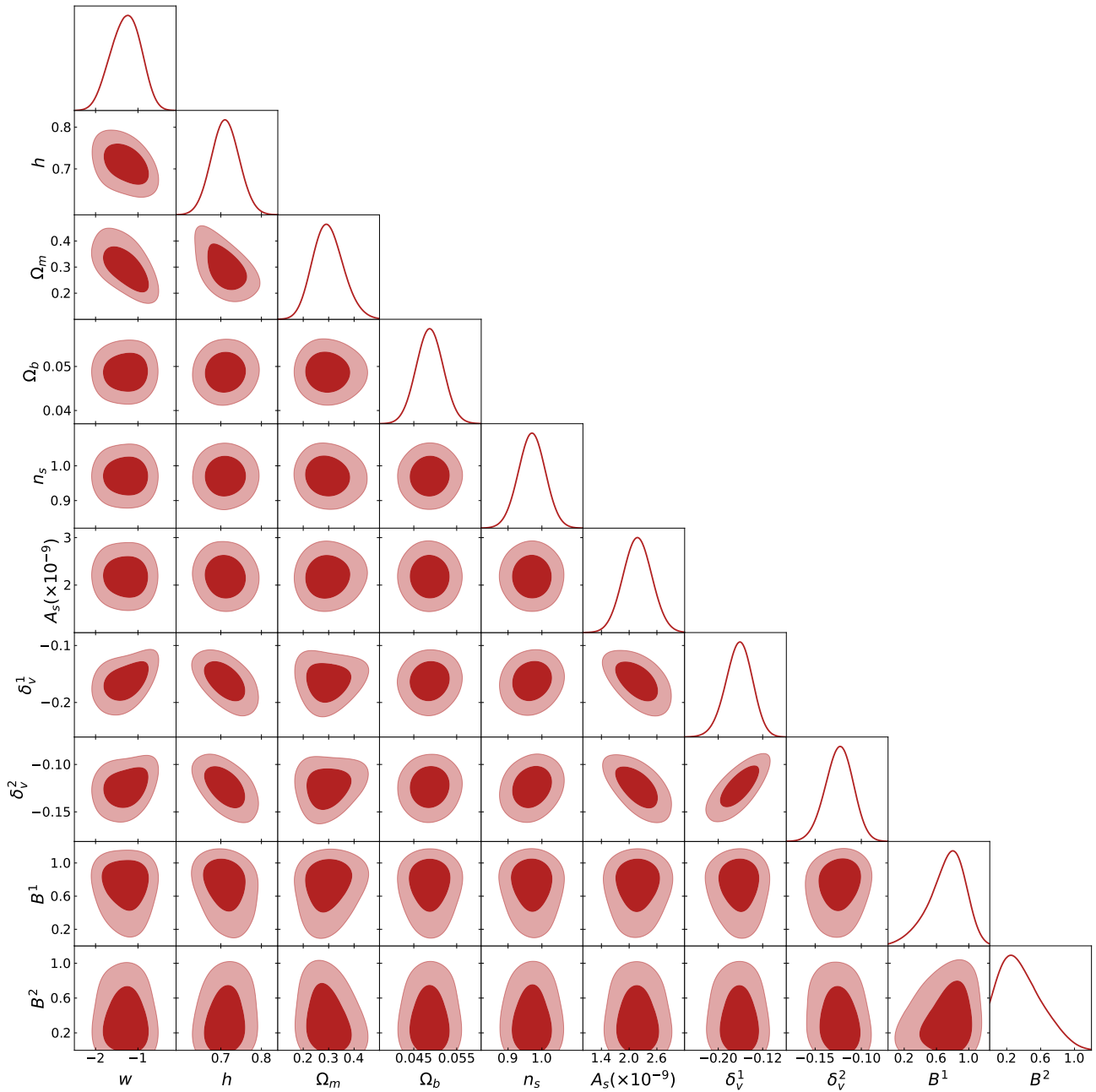


Figure A1. The 1D PDFs and contour maps at 68% and 95% CL for all the cosmological and void parameters in the model. The 10σ Gaussian priors have been applied to A_s , h , Ω_b , and n_s based on *Planck*2018 result in the fitting process.

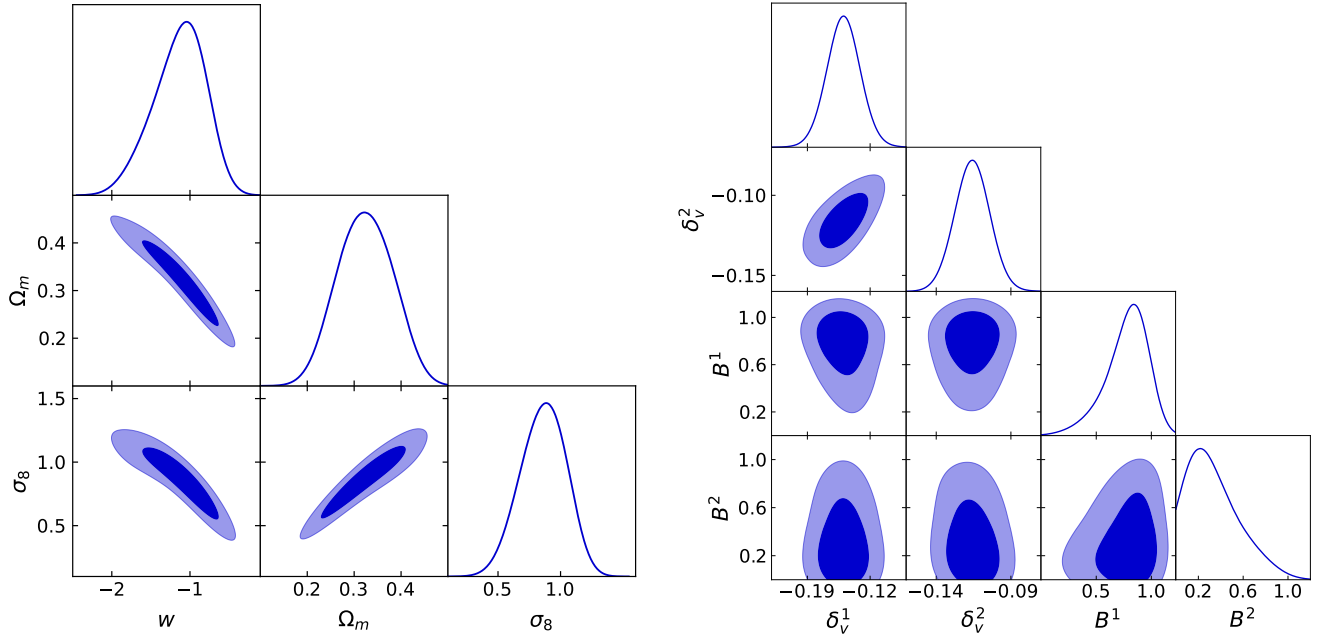


Figure A2. The 1D PDFs and contour maps at 68% and 95% CL for w , Ω_m and σ_8 (left panel), and δ_v^i and B^i in the two redshift bins (right panel). The 10σ Gaussian priors have been applied to A_s and the 1σ Gaussian priors are set to h , Ω_b , and n_s based on *Planck*2018 result in the fitting process.